Hydrodynamics of a single filament moving in a spherical membrane

Wenzheng Shi, Moslem Moradi, and Ehssan Nazockdast*
Department of Applied Physical Sciences, University of North Carolina at Chapel Hill, Chapel Hill, North Carolina 27599, USA

(Received 2 March 2022; accepted 5 July 2022; published 29 August 2022)

Dynamic organization of the cytoskeletal filaments and rodlike proteins in the cell membrane and other biological interfaces occurs in many cellular processes, including cell division, membrane transport, and morphogenesis. The filament dynamics are determined, in part, by their membrane-mediated hydrodynamic interactions. Previous modeling studies have considered the dynamics of a single rod on fluid planar membranes. We extend these studies to the more physiologically relevant case of a single filament moving in a *spherical* membrane. Specifically, we use a slender-body formulation to compute the translational and rotational resistance of a single filament of length L moving in a membrane of radius R and 2D viscosity η_m, and surrounded on its interior and exterior with Newtonian fluids of viscosities η^- and η^+. We first discuss the case where the filament's curvature is at its minimum $\kappa = 1/R$. We show that the boundedness of spherical geometry gives rise to flow confinement effects that increase in strength with increasing the ratio of filament's length to membrane radius L/R. These confinement flows result only in a mild increase in filament's resistance along its axis, $\xi_\parallel$, and its rotational resistance, ξ_Ω. As a result, our predictions of $\xi_\parallel$ and ξ_Ω can be quantitatively mapped to the results on a planar membrane, when the momentum transfer length scale is modified from $\ell_0 = (\eta^+ + \eta^-)/\eta_m$ in planar membranes to $\ell^\star = (\ell_0^{-1} + R^{-1})^{-1}$. In contrast, we find that the drag in the perpendicular direction, $\xi_\perp$, increases superlinearly with the filament's length when $L/R > 1$ and ultimately $\xi_\perp \to \infty$ as $L/R \to \pi$. Next, we consider the effect of the filament's curvature, κ, on its parallel motion, while fixing the membrane's radius. We show that the flow around the filament becomes increasingly more asymmetric with increasing its curvature. These flow asymmetries induce a net torque on the filament, coupling its parallel and rotational dynamics. This coupling becomes stronger with increasing L/R and κ.

DOI: 10.1103/PhysRevFluids.7.084004

I. INTRODUCTION

Many cellular processes involve the transport of rodlike proteins and biopolymers on curved fluidlike interfaces. One example is the continuous reorganization of the cell cortex made of the dynamic network of actin filaments [1], which determines the cell's mechanical integrity and drives cell division. Another example is the transport and organization of rodlike proteins that preferentially bind to areas of specific curvatures, such as septin oligomers [2] and BAR domains [3]. One required ingredient for simulating the dynamics of filaments in fluid membranes is the hydrodynamic resistance or mobility of a single filament. Moreover, mobility or resistance functions are typically needed to measure the interfacial rheology of the membrane from particles' motion in passive and active microrheology [4–7].

*ehssan@email.unc.edu

The first theoretical studies of the mobility of a membrane-bound particle go back to the works of Saffman and Delbrück [8] and Saffman [9] who calculated the mobility of a thin disk of radius a, bound to a planar membrane; the membrane is modeled as a 2D Newtonian fluid of viscosity η_m, and overlaying an infinitely bound Newtonian fluid of viscosity η. The mobility takes the form $\chi = (1/4\pi\eta_m)[\ln(2\ell_0/a) - \gamma]$, where $\gamma \approx 0.5772$ is Euler's constant and $\ell_0 = \eta_m/\eta \gg a$ is the length scale over which the momentum is transported from the membrane to the overlaying 3D fluid domain, referred to hereafter as Saffman-Delbrück (SD) length. Coupling the membrane and the overlaying fluid flows introduces SD length scale and, hence, removes the well-known Stokes paradox associated with solutions to 2D Stokes problems in free space. Note that for a particle significantly smaller than SD length, its dimensions affect the mobility through the weak logarithmic term $\ln(2\ell_0/a)$. Some experimental studies on the dynamics of membrane-bound proteins [10,11] have found good agreement between Saffman's predictions and experiments, while others [12] found the mobility to scale inversely with particle size. These disagreements were consequently described by models that account for the additional flow dissipation due to local deformation of the membrane induced by interactions with the bound particle [13] and membrane structure and mechanics [14–16].

Evans and Sackmann [17] and Stone and Ajdari [18] considered the case of a disk bound to a planar membrane overlaying a 3D fluid domain of finite depth. These studies show that the momentum transfer from the membrane to the 3D fluid domain occurs at length-scale $\ell_H = \sqrt{\ell_0 H}$, where H is the 3D fluid depth. Oppenheimer and Diamant [19] studied the hydrodynamic interactions (HIs) between two Brownian disks in the same system. Oppenheimer *et al.* [20] extended this analysis to a suspension of rotors and showed that the suspension can crystallize by a combination of hydrodynamic and steric interactions between the particles while ignoring any of these interactions does not lead to crystallization. Manikantan [21] numerically studied particles with a force dipole acting on them, as a model for membrane-bound active particles. Their results show that large-scale particle aggregation can be controlled by tuning the depth of the surrounding 3D fluid domain.

Levine *et al.* [22] considered the mobility of a rodlike particle moving with a constant translational and rotational velocity in a planar membrane. The authors used a slender-body formulation and the fundamental solutions to a point force on a planar membrane (planar Green's function) to describe the disturbance flows induced by the filament's motion. They found that for $L/\ell_0 \ll 1$, the drag coefficient is independent of rod orientation and asymptotes to SD results for a disk of radius L. When $L/\ell_0 \gg 1$, the drag coefficient in parallel direction retains the logarithmic correction that is observed in 3D flows: $\xi_\parallel/(4\pi\eta_m) \approx 0.25(L/\ell_0)[\ln(0.43L/\ell_0)]^{-1}$, with the difference that the effective filament radius is now ℓ_0, rather than the physical radius a. In contrast, the drag coefficient in the perpendicular direction becomes purely linear in length, $\xi_\perp/(4\pi\eta_m) \approx 0.25(L/\ell_0)$, and significantly larger than the parallel drag. In comparison, the ratio of perpendicular to the parallel drag of filaments in 3D flow is nearly two. These predictions were corroborated with microrheological measurements of the translational and rotational drags over the range of $0.01 \leqslant L/\ell_0 \leqslant 10$ [23].

This qualitative difference between a 2D membrane and a 3D fluid domain can be understood by noting that the planar Green's function along the direction of the applied force and perpendicular to it, when $L/\ell_0 \gg 1$, decay as $G_\parallel \sim 1/\tilde{r}$ and $G_\perp \sim 1/\tilde{r}^2$, respectively, where $\tilde{r} = r/\ell_0$ is the dimensionless distance from the applied force (in comparison, the 3D Green's function decays as $1/r$ in both directions). Thus, when $L/\ell_0 \gg 1$, the filament's mobility scales with $\chi_{(\parallel,\perp)} \sim (\ell_0/L)\int_1^{L/\ell_0} G_{(\parallel,\perp)}(\tilde{r})\, d\tilde{r}$. This leads to a logarithmic contribution in the parallel direction and a constant in the perpendicular direction (free draining limit), when $L/\ell_0 \gg 1$ [24].

Fischer [25] and Verwijlen *et al.* [6] extended the work of Levine *et al.* [22] to study the dynamics of rodlike inclusions in membranes overlaying a fluid domain of finite depth, and explored the consequences of this finite depth on the accuracy of interfacial rheological measurements.

Membranes are typically curved in biological and synthetic applications. The membrane's curvature and topology produce novel features in the interface-bound transport processes that make it distinct from a planar membrane [26–31]. Different statistical mechanical aspects of curved

membranes are surveyed in [32]. Most studies on the dynamics of inclusions bound to the membrane are done on planar membranes, and the number of studies on curved membranes is in comparison small [33,34]. In the special cases of spherical and cylindrical membranes, the Gaussian curvature remains constant over the surface. This greatly simplifies the equations, allowing for analytical calculations of fundamental solutions to a point force, a point torque, and a torque dipole [35–37]. These fundamental solutions can be used to describe the flow disturbances due to the presence of other bodies in the membrane, which is similar to the singular methods for 3D Stokes flow suspensions [38,39]. This is also the methodology used in this study.

Henle and Levine [36] studied the translational mobility of a disklike inclusion of radius a on *nondeformable* spherical and cylindrical membranes of radius R. In the limit of small curvature $R/\ell_0 \gg 1$, one recovers the planar membrane results. At larger curvatures $R/\ell_0 \ll 1$, the mobility is reduced with the logarithmic term now being defined as $\ln(R/a)$ in contrast to $\ln(\ell_0/a)$ on planar membranes. In a recent study, Samanta and Oppenheimer [37] used the same framework to study the effect of the membrane curvature on the hydrodynamic interactions (HIs) and the ensued nonlinear dynamics of rotors bound to spherical membranes. Bagaria and Samanta [40] investigated the curvature confinement effect on the aggregation of force dipoles on the spherical membranes.

The current study extends the work of Levine *et al.* [22] to filaments moving in spherical membranes. Specifically, we consider the case of a filament of length L and constant curvature, κ, along its axis, moving in a membrane of radius R with 2D viscosity η_m, and surrounded by the interior and exterior Newtonian fluids of viscosities η^- and η^+, where the SD length is redefined as $\ell_0 = \eta_m/(\eta^+ + \eta^-)$. In Sec. IV A we study the filament's drag when its curvature is at its minimum $\kappa_{\min} = 1/R$. This is the filament's likely conformation when the characteristic bending forces are comparable to filament-membrane interaction forces in the radial direction and both are significantly larger than the thermal forces. We use a slender-body formulation to compute the filament's drag coefficients along its axis, $\xi_\parallel$, and perpendicular to it, $\xi_\perp$, as well as its rotational drag coefficient, ξ_Ω in a wide range of ℓ_0/R, and L/R.

When membrane radius is much larger than SD length, $\ell_0/R \ll 1$, the filament's dynamics become independent of the membrane radius and our results approach those of a planar membrane given by Levine *et al.* [22]. In the opposite limit of $\ell_0/R \gg 1$, the momentum transfer to the overlaying fluid domain occurs over the membrane's radius R, and the dynamics become independent of ℓ_0. Here, we find that the transnational resistance in the direction parallel to the filament and the rotational resistance closely follow the results of a planar membrane, if SD length is replaced with the membrane radius. In contrast, the resistance in the perpendicular direction, $\xi_\perp$, shows strong positive deviations from the planar membrane results. We show that these deviations arise due to flow confinement effects on a spherical membrane, which has no analog in free 2D planar membranes. As a result, $\xi_\perp$ strongly increases with the filament's length when $L/R \sim O(1)$, and $\xi_\perp \to \infty$ as $L/R \to \pi$.

In Sec. IV B we study the effect of the filament's curvature on its dynamics. The motivation for studying this problem is to model the dynamics of rodlike biopolymers with an intrinsic (preferred) curvature, which preferentially bind to areas of the membrane that match their curvature. One example includes the crescent-shaped BAR domains that play a key role in inducing and sensing membrane curvature in cellular processes [3]. We present the filament with curvature κ by aligning it along the azimuthal direction of the spherical membrane and placing it at a distance $h = \sqrt{R^2 - \kappa^{-2}}$ from the equator in the z direction. We show that the filament's motion along its axis produces asymmetric flows, resulting in a net torque on the filament. This coupling between parallel and rotational motion is increased with the filament's length and curvature.

II. FORMULATION

We consider the motion of a filament with length L and *constant curvature* along its length, bound to a fixed (undeformable) spherical membrane of radius R and Newtonian viscosity η_m. Due to spherical symmetry, any configuration of a filament with constant curvature can be mapped into

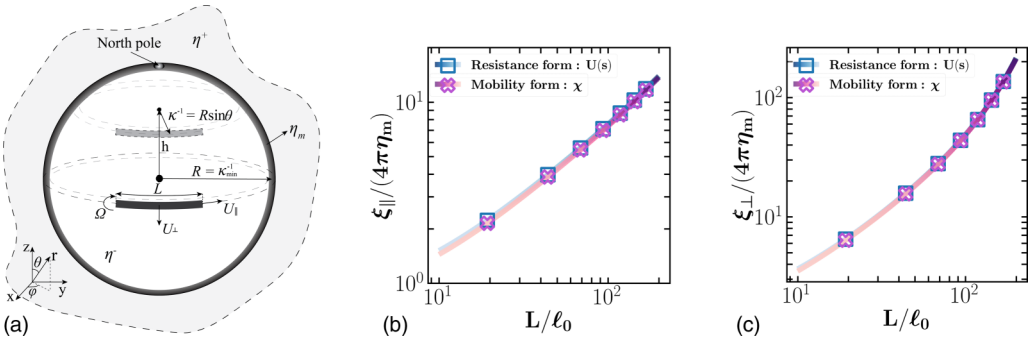

FIG. 1. (a) An illustration of the filament motion on a spherical membrane of viscosity η_m and surrounded on the interior and exterior sides by 3D fluid domains of shear viscosities η^- and η^+. The filament dynamics is described by three modes of motion: translation along and perpendicular to its axis ($U_\parallel$ and $U_\perp$), and rotation (Ω). The filament's curvature is at its minimum when it is aligned along the equator ($\kappa_{\min} = R^{-1}$). The results of this configuration are presented in Sec. IV A. To model filaments of curvature $\kappa > \kappa_{\min}$, they are placed at distance $h = \pm\sqrt{R^2 - \kappa^{-2}}$ away from the equator. This configuration is studied in Sec, IV B. (b, c) The dimensionless resistance of a filament translating in parallel (b) and perpendicular (c) directions as a function of L/ℓ_0, where $\ell_0/R = 0.01$. The blue line (square dots) shows the result of the numerical solutions to the resistance formulation given by $\mathbf{U}(s)$, Eq. (4), while the red line (cross dots) shows the numerical integration of the mobility formulation given by $\boldsymbol{\chi}$, Eq. (5), assuming a constant force density along the filament. The results are in excellent agreement with each other.

the filament being aligned along the azimuthal direction and with a distance h along the z axis, which is shown in Fig. 1(a). The filament's curvature is at its minimum, $\kappa_{\min} = 1/R$, when it is placed on the equator ($h = 0$). This is the most likely conformation of the filament if the filament does not have an intrinsic curvature and the characteristic bending or elastic forces are significantly larger than thermal forces. We begin by studying the dynamics in this limit in Sec. IV A. Due to geometric and flow symmetries, the translational and rotational modes of motion of the filament are decoupled. Thus, the translational resistance tensor can be generally defined as $\boldsymbol{\xi} = \xi_\parallel \mathbf{qq} + \xi_\perp(\mathbf{I} - \mathbf{qq})$, where $\mathbf{I}$ is the identity matrix and $\mathbf{q}$ is the unit vector along the filament main axis.

As shown in Fig. 1(a), the general case of a filament with curvature $\kappa > 1/R$ is equivalent to placing the filament at $h = \pm\sqrt{R^2 - \kappa^{-2}}$ away from the equator and aligned along the azimuthal direction ϕ, which corresponds to constant polar angle $\theta = \arcsin(\kappa R)^{-1}$. Moving the filament along its axis produced asymmetric flows, and net torque on the filament, resulting in the coupling of the filament's parallel and rotational motion. This is discussed in Sec. IV B.

We use a slender-body formulation to model the flow disturbances induced by the filament with a distribution of force densities, $\mathbf{f}(s)$, along the filament's length:

$$\mathbf{u}(\mathbf{x}_m) = \int_{-L/2}^{L/2} \mathbf{G}(\mathbf{x}_m, \mathbf{x}_m^0(s)) \cdot \mathbf{f}(s)\, ds, \tag{1}$$

where $s \in [-L/2, L/2]$ denotes the filament's arclength, $\mathbf{x}_m$ and $\mathbf{x}_m^0$ are points on the membrane surface, and $\mathbf{G}(\mathbf{x}_m, \mathbf{x}_m^0(s))$ is the Green's function of membrane-3D fluids coupled system in response to a point-force applied on the membrane at position $\mathbf{x}_m^0$. Note that the Green's function scales as $\ln|s - s'|$ when $s - s' \to 0$, and thus diverges as $|s - s'| \to 0$. But our resolution studies presented in the Supplemental Material show that the integrals are numerically convergent and no further regularization is needed [41].

Assuming flow incompressibility on the membrane surface and the adjacent 3D flows and negligible inertia, the associated momentum and continuity equation for the membrane and 3D fluid domains are [36,37]

$$\text{3D fluids:} \quad \eta^{\pm}\nabla^2\mathbf{u}^{\pm} - \nabla p^{\pm} = \mathbf{0}, \quad \nabla\cdot\mathbf{u}^{\pm} = 0, \tag{2a}$$

$$\text{Membrane:} \quad \eta_m(\Delta_\gamma\mathbf{u}_m + K(\mathbf{x}_m)\mathbf{u}_m) - \nabla_\gamma p_m + \mathbf{T}|_{r=R} = \mathbf{0}, \quad \nabla_\gamma\cdot\mathbf{u}_m = 0, \tag{2b}$$

where $\mathbf{u}^{\pm}$ and $p^{\pm}$ are the velocity and pressure fields in 3D fluid domains, and $\mathbf{u}_m$ and p_m are the velocity and pressure fields in the membrane; Δ_γ and ∇_γ are the surface (defined by γ) Laplacian and divergence operators, $K(\mathbf{x}_m)$ is the local Gaussian curvature of the surface, and $\mathbf{T}|_{r=R} = [\boldsymbol{\sigma}^{+}(\mathbf{x}_m) - \boldsymbol{\sigma}^{-}(\mathbf{x}_m)]\cdot\mathbf{n}(\mathbf{x}_m)$ is the traction applied from the surrounding 3D fluid domains on the membrane, where $\boldsymbol{\sigma}^{\pm}$ denotes the 3D fluid stress and $\mathbf{n}(\mathbf{x}_m)$ is the surface normal vector pointing towards the exterior domain.

The coupling between the membrane and 3D flows is enforced by the continuity of forces and velocities across the membrane surface. The force continuity is already imposed through including the traction term, $\mathbf{T}|_{r=R}$, in Eq. (2b). The radial velocity is zero at $r = R$, for a fixed spherical membrane, which results in $u_r^{\pm} = 0$ throughout both 3D fluid domains. Other boundary conditions (BCs) for 3D flows include velocities decaying to zero on the exterior domain, $\lim_{r\to\infty} u^{+}_{\theta,\phi}(r) \to 0$. Finally, requiring the velocity and stress fields to be finite at the interior domain's center, $r = 0$, provides sufficient BCs.

The Gaussian curvature of a sphere is a constant, $K(x) = R^{-2}$, which greatly simplifies Eqs. (2), allowing one to obtain analytical solutions for Green's function in terms of the position of the applied force (θ_0, ϕ_0) and an arbitrary target point on the sphere (θ, ϕ). Here $\theta \in [0, \pi]$ and $\phi \in (0, 2\pi]$ are the polar and azimuthal angles in spherical coordinate. The detailed derivation of the Green's function is outlined in [36] and [37]. The expressions for all components of the Green's function ($G_{\theta\theta}$, $G_{\theta\phi}$, $G_{\phi\theta}$, $G_{\phi\phi}$) are provided in the Appendix for completeness.

To calculate the resistance in parallel ($\xi_\parallel$) and perpendicular ($\xi_\perp$) directions, we set the filament velocity as a constant in each direction and compute the distribution of force density on the filament by solving the following integral equation:

$$\mathbf{U}(s) = \int_{-L/2}^{L/2} \mathbf{G}(\mathbf{X}(s) - \mathbf{X}(s'))\cdot\mathbf{f}(s')\,ds', \tag{3}$$

where $\mathbf{X}(s)$ is a point located at s arclength of the filament. Equation (3) is a Fredholm integral equation of the first kind. This class of integral equations are known to be ill-posed leading to a loss of convergence and numerical inaccuracy. To circumvent this issue we use a regularization technique, analogous to those used in nonlocal slender-body theories of filaments moving in 3D fluid domains [42,43], to transform the equation to a second-kind Fredholm integral equation, which can then be accurately solved using different numerical integration techniques.

We divide the domain of integration into a short local domain around s, $\Upsilon_{\mathrm{L}}(s') = [s - \frac{\delta L}{2},\ s + \frac{\delta L}{2}]$ and the remainder of the filament length, $\Upsilon_{\mathrm{NL}}(s') = [-\frac{L}{2}, s - \frac{\delta L}{2}) \cup (s + \frac{\delta L}{2}, \frac{L}{2}]$, where $\frac{\delta L}{L} \ll 1$, $\frac{\delta L}{R} \ll 1$ and "L" and "NL" correspond to the local and nonlocal domains [44]. The local domain near the ends of the filament modifies to $\Upsilon_{\mathrm{L}}(s') = [\frac{L}{2} - \delta L,\ \frac{L}{2}]$ and $\Upsilon_{\mathrm{L}}(s') = [-\frac{L}{2},\ -\frac{L}{2} + \delta L]$. Next, we assume the force density remains uniform within the local domain: $\mathbf{f}(s') \approx \mathbf{f}(s)$. The modified integral equation is

$$\mathbf{U}(s) = \int_{\Upsilon_{\mathrm{NL}}} \mathbf{G}(\mathbf{X}(s) - \mathbf{X}(s'))\cdot\mathbf{f}(s')\,ds' + \left\{\int_{\Upsilon_{\mathrm{L}}} \mathbf{G}(\mathbf{X}(s) - \mathbf{X}(s'))\,ds'\right\}\cdot\mathbf{f}(s). \tag{4}$$

The second term on the right-hand side makes Eq. (4) a second kind Fredholm integral equation, which can be solved by collocation methods described briefly in Sec. III. The computed force density is, then, integrated to obtain the total force on the rod. The resistance is determined by taking the ratio of this force to velocity in $\parallel$ and $\perp$ directions.

The rotational resistance can also be computed using the same formulation with the difference that the set velocity corresponds to a pure rotational motion: $\mathbf{U}_\Omega(\mathbf{X}(s)) = \Omega s \mathbf{q}_\perp$, where Ω is the angular rotation, and $\mathbf{q}_\perp$ is the filament's transverse direction. The rotational resistance is the ratio of torque to angular rotation.

III. NUMERICAL IMPLEMENTATION

We solve for the force distribution in Eq. (4), by discretizing the rod into N equally spaced points and using trapezoidal integration. This leads to N linear system of equations in the matrix form $\mathcal{U} = \mathcal{A} \cdot \mathcal{F}$, where $\mathcal{U}$ is the $N \times 1$ array representing unit velocities along the rod at a given direction, $\mathcal{A}$ is the $N \times N$ matrix representing the HIs, and $\mathcal{F}$ is the unknown forces along the rod. We solve this system using direct solution methods. The computed forces are then integrated to give the resistance in parallel and perpendicular directions.

The length of the local domain is set to $\frac{\delta L}{L} = \frac{1}{30}$, for all the results presented here. Varying this length in the range $10^{-2} \leqslant \frac{\delta L}{L} \leqslant 10^{-1}$ changed the results by less than 5%. Resolution studies at a given δL show that our method is second-order accurate. These results are provided in Supplemental Material [41]. The reported results were obtained using $N = 1021$ discretization points. The computations can be made far more efficient requiring less number of points, but we defer this to future studies.

The rotational resistance can be computed in an analogous way, i.e., after computing the force distribution corresponding to a rotational motion of the filament, we compute the total torque, and its ratio to the angular velocity.

A consequence of the slenderness of rods is that the force density remains nearly uniform throughout the length of the rod in 3D flows for translational motion, except near its two ends. For rotational motion the force density varies linearly with arclength, changing the sign at the center of mass, $s = 0$. The end effects determine the next order corrections to the mobility or resistance, which depend on the detailed treatment of the rod geometry, e.g., assuming the rod is tapered or not [45]. Thus, instead of solving a linear system of equations, one can obtain the leading order form of the mobility (or resistance) tensor, by assuming the force is uniform along the rod and simply evaluating the mobility as the ratio of the mean velocity to the total force. The equation for translational mobility is

$$\boldsymbol{\chi} = L^{-2} \int_{-L/2}^{L/2} ds \int_{-L/2}^{L/2} \mathbf{G}(\mathbf{X}(s) - \mathbf{X}(s'))ds'. \tag{5}$$

Inverting the mobility tensor gives the resistance tensor: $\boldsymbol{\xi} = \boldsymbol{\chi}^{-1}$. Figures 1(b) and 1(c) show the predictions of the dimensionless resistance tensor in parallel and perpendicular directions as a function of L/ℓ_0 when $\ell_0/R = 0.01$ by solving Eq. (4) and Eq. (5). The predictions from the two methods are close with no more than 10% and 20% difference in the parallel and perpendicular direction, respectively, for all the parameters space we have investigated. We provide a detailed analysis of the difference between the two methods in the Supplemental Material [41]. All the results reported hereafter were computed using Eq. (4).

Finally, we note that for all the results presented hereafter we set $\eta^+/\eta^- = 1$. Varying this ratio produced only rather small $O(1)$ changes in the final results and, thus, were not explored here to focus on large variations of the drag induced by flow confinements.

IV. RESULTS

A. Filament placed on the equator ($\kappa = \kappa_{\min} = R^{-1}$)

We begin by presenting the results of the filament at its minimum curvature $\kappa_{\min} = 1/R$. We note that applying a net force on filament bound to the spherical membrane produces a net torque on the membrane, which leads to a net rotational flow of the entire system [36]. This effect is

absent in a planar membrane [37]. The resistance and mobility functions are defined based on the *relative* velocity of the filament with respect to the ambient fluid. As such, we subtract this rigid-body rotation from the velocity field of a moving filament in our computations of the resistance functions and surface flows. The same implementation was used by Henle and Levine [36]. The implementation details are provided in Appendix.

The filament's dynamics on a planar membrane are defined by two lengths: the filament's length, L, and SD length, ℓ_0. Spherical geometry introduces another length: R. Constant filament curvature imposes an upper bound on its length: $L < 2\pi R$. We assume that the filament thickness, a, is significantly smaller than all other length scales. The filament is modeled as a line with no thickness in the results presented here. In the Supplemental Material, we show that the relative change in the computed resistance functions due to finite thickness of the filament at most scales with $O(\epsilon)$, where $\epsilon = a/L$; hence, filament thickness has a negligible effect on the computed hydrodynamic functions [41].

We study translational resistance, in parallel and perpendicular directions, and rotational resistance in three regimes: $\ell_0/R \ll 1$, $\ell_0/R \sim O(1)$, and $\ell_0/R \gg 1$. The results are presented in Fig. 2. In all cases the variations of the resistance are presented as the length of the filament is changed, while fixing ℓ_0/R. Thus, L/R varies in each individual line in Fig. 2. These variations are visualized by varying the transparency of each color in the plot from more transparent (lighter) in smaller L/R to less transparent (darker) in larger L/R.

As shown in Fig. 2(a), in the limit of $\ell_0/R \ll 1$ the resistance plots in a parallel direction for different values of ℓ_0/R nearly collapse to the resistance values of a planar membrane at $L/R \ll 1$, and show relatively weak positive deviations which are at most 40% from this curve. The positive deviations result from the flow confinement effects in a closed spherical geometry and, thus, increase with L/R. The details are provided in the Supplemental Material [41].

In the opposite limit of $\ell_0/R \gg 1$, shown in Fig. 2(b), the resistance (and mobility) become independent of ℓ_0, resulting in a nearly perfect collapse of all the results when plotted against L/R. Both limits can be understood by noting that the length scale that determines the flows and the hydrodynamic functions is the length scale over which the momentum is transported from the membrane to the surrounding 3D fluid domains, which we refer to as $\ell^\star$ hereafter. In the case of $\ell_0/R \ll 1$, the momentum transport occurs in $\ell^\star = \ell_0$, and the results closely follow those of a planar membrane. In the other limit of $\ell_0/R \gg 1$, the momentum transfer occurs over the dimension of the spherical geometry, R, which is smaller than ℓ_0. As such, the results are independent of ℓ_0.

Based on this understanding, we combine the results of Figs. 2(a) and 2(b) into Figs. 2(c), by rescaling the length in $x-$ axis with $\ell^\star = (\ell_0^{-1} + R^{-1})^{-1}$, which asymptotes to the expected limits. With this rescaling, the computed parallel resistance for a wide range of ℓ_0/R collapse to its planar membrane values when $L/R < 1$ (lighter colors), and shows weak positive deviations at larger L/R values.

Figures 2(d), 2(e), and 2(f) present the rotational resistance at the same limits as the parallel motion. As it can be seen, similar to the parallel resistance, the rotational resistance closely matched that of a planar membrane, when the filament's length is appropriately made dimensionless by $\ell^\star$.

Finally, in 2(g), 2(h), and 2(i) we present the variations of translational drag in perpendicular direction as a function of the filament's length in the same regimes. When $\ell_0/R \ll 1$ and $L/R \ll 1$, the computed drag coefficients converge to the planar membrane values. In contrast to the parallel and rotational drag, we observe strong positive deviations from the planar membrane results with increasing L/R. This demonstrates that flow confinement has a significantly stronger effect on $\xi_\perp$ than $\xi_\parallel$ and ξ_Ω. In the limit of $\ell_0/R \gg 1$, similar to the previous cases, the dynamics become independent of ℓ_0, resulting in the collapse of all data when plotted against L/R. However, these variations are significantly stronger than those in parallel and rotational resistance functions. As expected rescaling the length with $\ell^\star$ cannot collapse the data. Note that to move in the perpendicular direction and to remain bound to the membrane, the filament needs to deform and change its curvature. These deformations are induced by membrane-filament interactions in the radial direction and produce no

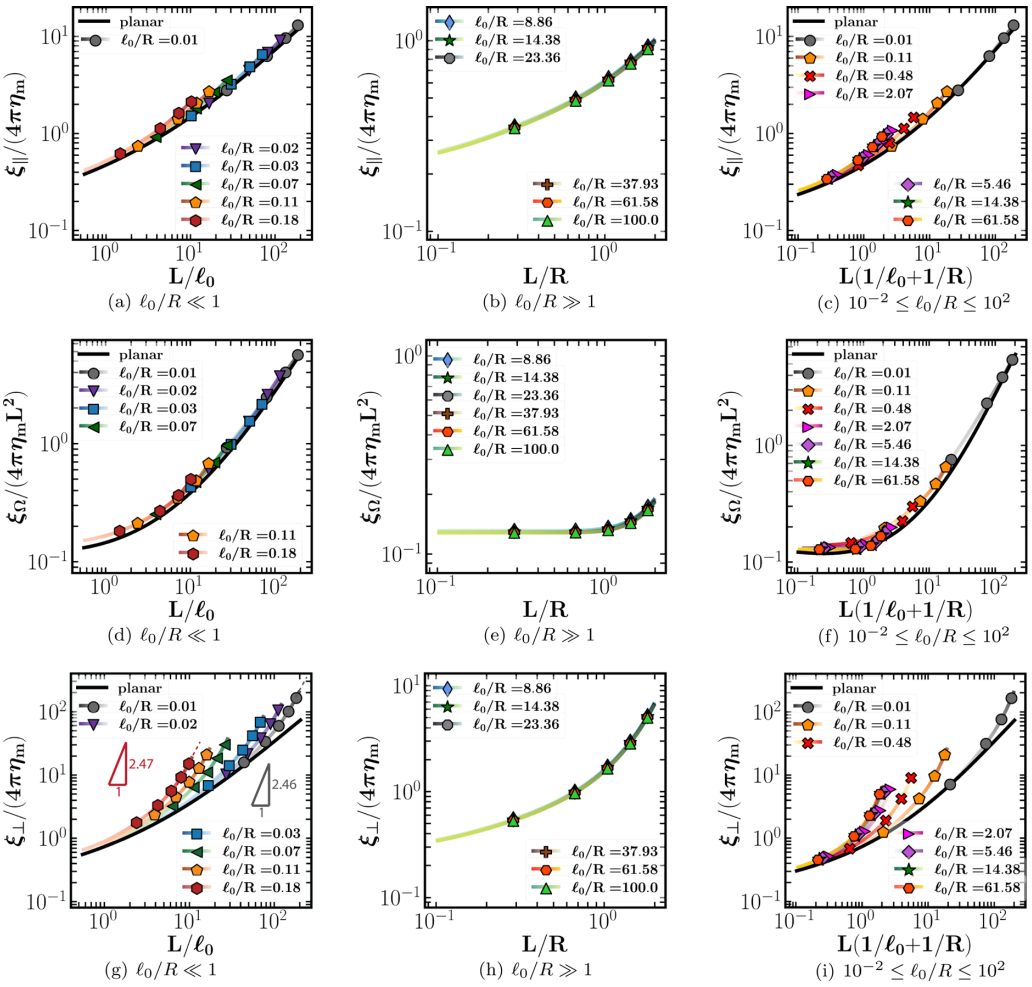

FIG. 2. The parallel(upper row), perpendicular(lower row) and rotational(middle row) resistance as a function of L/ℓ_0 and L/R in different limits of ℓ_0/R. The left column and middle column correspond to $\ell_0 \ll R$ and $\ell_0 \gg R$, respectively. The right column includes all data in the range $10^{-2} \leqslant \ell_0/R \leqslant 10^2$. The solid black lines in (a), (c), (d), (f), (g), and (i) represent the associated resistance values in planar membranes [22]. The variations of L/R for each choice of ℓ_0/R are visualized by changing the color from light (left end of each plot) to dark (right end of each plot) with increasing L/R.

net force on the surface of the sphere. Thus, the computed instantaneous perpendicular resistance remains unchanged by these deformations.

Figure 3(a) shows the flow generated by a point force placed on the equator and pointing towards the south pole. Note that we have subtracted the flows due to the pure rotational motion of the membrane and surrounding fluids, as discussed earlier in this section. As it can be seen, the boundedness of spherical geometry produces strong flow reversal and re-circulation regions as we move in the direction perpendicular to the point force ($\hat{\phi}$), whereas the flows remain parallel to the point force, when moving in the direction parallel to the force ($\hat{\theta}$).

Figure 3(b) shows the velocity fields induced by the filament's motion in the perpendicular direction. The flows are qualitatively similar to the flow induced by a point force with the difference that the flow reversal regions are now pushed to areas near the filament's ends. As we discussed

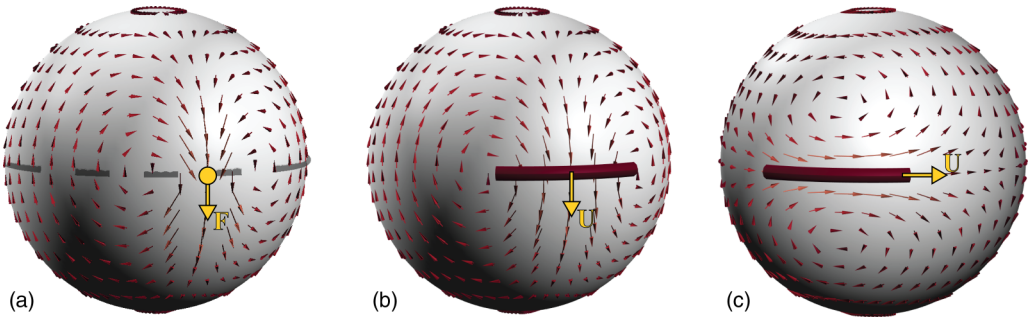

FIG. 3. (a) The flow field induced by a point force in the perpendicular direction at $(\theta = \pi/2, \phi = 0)$ for the choice of $\ell_0/R = 1$. (b) The flow field induced by a filament moving with a constant velocity in the perpendicular direction for the choice of $\ell_0/R = 1$ and $L/R = 1$. (c) The flow field induced by a filament moving with a constant velocity in the parallel direction for the choice of $\ell_0/R = 1$ and $L/R = 1$.

in Sec. III, a filament moving with a constant velocity can be modeled as a collection of smaller segments all moving with the same velocity, where the coupling between the segments is through their HIs. The flow generated by a segment is similar to the flow due to a point force, shown in Fig. 3(a). Thus, when the filament is moving in the perpendicular direction, the motion of one segment can generate flows pointing in the opposite direction of motion on other segments, i.e., HIs cause anticorrelated motions. As a result, more force is needed to maintain the same velocity across all segments, leading to an increase in the total drag compared to the free draining limit.

Figure 3(c) shows the velocity field induced by the filament's parallel motion. In this case, the motion of a segment produces flows in the same direction as the motion on other filament's segments, i.e., HIs cause correlated motion, leading to a reduction in the total drag, compared to the free draining limit.

In Fig. 4(a) we quantify these variations of surface velocity in the perpendicular direction along the equator, and at different filament lengths. The results are obtained for the choice of $\ell_0/R = 1$;

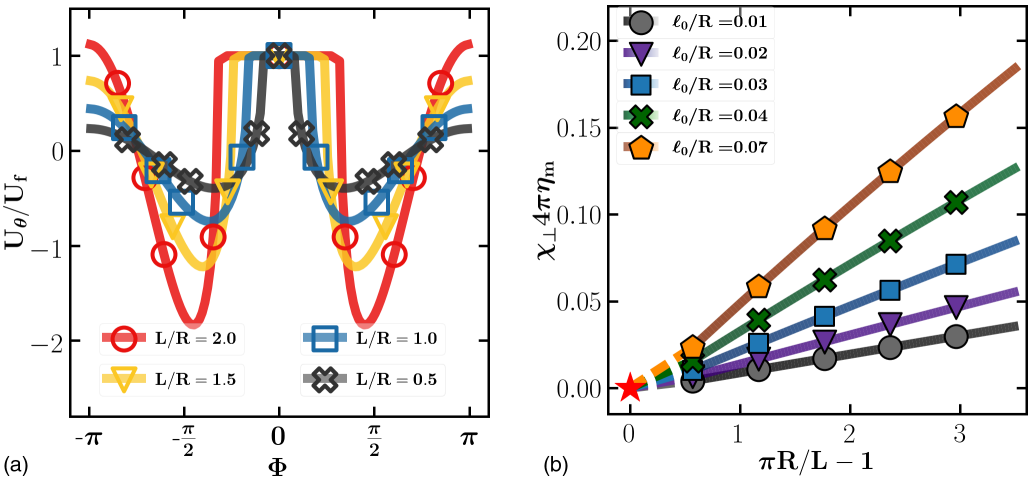

FIG. 4. (a) The polar velocity distributed in the azimuthal direction along the equator, normalized by the filament velocity for the choice of $\ell_0/R = 1$. The different colors and symbols represent different ratios of L/R. (b) The mobility of filament in the perpendicular direction as a function of gap distance, $\pi R/L - 1$, for different values of ℓ_0/R.

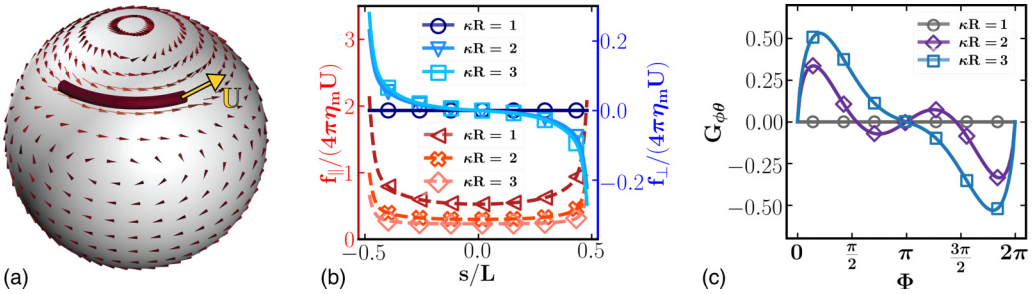

FIG. 5. (a) The flow field induced by the parallel motion of a filament placed at $h = R/\sqrt{2}$ away from the equator ($\kappa = \sqrt{2}R^{-1}$), when $\ell_0/R = 1$ and $L/R = 1$. (b) The distribution of force per unit length along the filament in parallel and perpendicular directions ($\mathbf{f}_{\parallel,\perp}$) at different latitudes (curvatures), when $\ell_0/R = 1$ and $L/R = 1$. (c) Variations of $G_{\phi\theta}$ vs ϕ, at different latitudes or curvatures (θ_0), when the source point is located at ($\theta_0, \phi_0 = 0$) and the target is at (θ_0, ϕ). The results are presented for $\ell_0/R = 1$; see the Appendix for the full expression of Green's function.

again, we have removed the pure rotation component of the velocity field. The flow gradients are the strongest near the filament's ends, and they strongly increase with the filament's length. These flow gradients result in large traction forces near the filament's ends and a strong increase in the total drag.

Figure 4(b) shows the perpendicular mobility $\chi_\perp = \xi_\perp^{-1}$ as a function of the gap size, for different values of ℓ_0/R, where we define the gap size as the distance between the membrane's half-perimeter and filament's length, $\pi R/L - 1$, which is nondimensionalized by filament length. In all plots the mobility approaches zero, $\chi_\perp \to 0$, corresponding to $\xi_\perp \to \infty$, as $L \to \pi R$. These results are in line with the results of Figs. 2(g) and 4(a), demonstrating the rapid growth of $\xi_\perp$ with the filament's length when $L/R > 1$. Obtaining the asymptotic form of mobility requires a more in-depth analysis and careful numerical evaluations, which we do not pursue in this study.

B. Filament placed away from the equator ($\kappa > R^{-1}$)

Thus far we have focused on the case where the filament's curvature is at its minimum, $\kappa_{\min} = 1/R$. Next, we ask how changing the filament's curvature, independently of the membrane geometry, affects its dynamics. This introduces another dimensionless parameter κR, which is the ratio of filament's curvature to its minimum allowed curvature on that membrane. Due to the mismatch between the membrane and filament curvatures, the filament cannot undergo pure rotational motion, while remaining bound to the membrane. The same conditions apply to motion along the perpendicular direction, which makes defining and computing ξ_R and $\xi_\perp$ problematic when $\kappa \neq 1/R$. Because of this complexity, we focus only on the well-defined dynamics in the parallel direction.

Figure 5(a) shows the surface fluid flows induced by the parallel motion of a filament placed between the equator and the north pole, when $\ell_0/R = 1$ and $L/R = 1$ and $\kappa R = \sqrt{2}$. As expected, the flows are asymmetric around the filament. This flow asymmetry produces a nonzero distribution of forces along the filament in perpendicular directions, $f_\perp$, which are shown in Fig. 5(b) for different values of κR. Note that the parallel force distribution remains uniform (except near the ends) and symmetric around the filament's midpoint ($s = 0$), while the perpendicular force is antisymmetric around $s = 0$ and increases in magnitude as the filament nears the pole. The total torque normal to the spherical boundary scales with $\int_{-L/2}^{L/2} s f_\perp \, ds$. The integrand is an even function, resulting in a nonzero torque on the filament.[1] In other words, placing the filament away from the

[1]This torque changes sign as the filament is placed on the southern hemisphere.

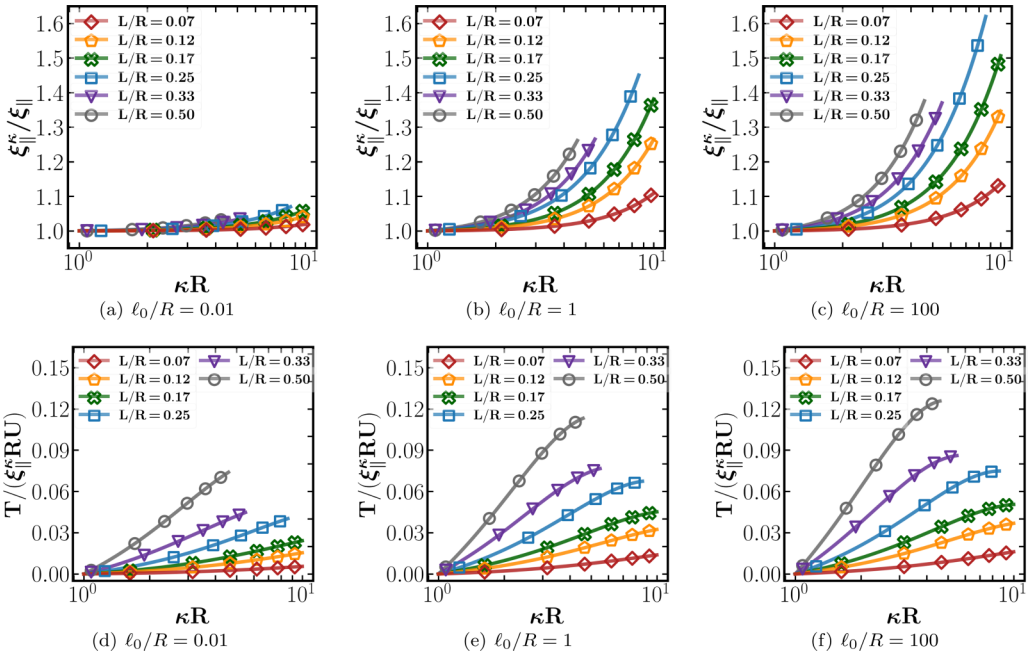

FIG. 6. Top row (a–c)" The resistance along the parallel direction vs the filament's dimensionless curvature (κR) for $0.07 \leqslant L/R \leqslant 0.50$ at (a) $\ell_0/R = 0.01$, (b) $\ell_0/R = 1$, and (c) $\ell_0/R = 100$. When $\ell_0/R \ll 1$ the parallel resistance remains nearly constant with curvature and equal to the results at the equator. When $\ell_0/R \geqslant 1$, the resistance monotonically increases with curvature, and the rate of this increase is amplified with increasing L/R. Bottom row (d–f): the net torque induced on the filament by its motion in the parallel direction as a function of the filament's dimensionless curvature for the range $0.07 \leqslant L/R \leqslant 0.50$ at (d) $\ell_0/R = 0.01$, (e) $\ell_0/R = 1$, and (f) $\ell_0/R = 100$. The torque magnitude is nondimensionalized by the external force moment on the membrane: $\xi_{\parallel}^{\kappa} RU$. Regardless of the choice of ℓ_0/R, the torque monotonically increases with κR; this effect is amplified with increasing L/R. The results appear to be a weak function of ℓ_0/R, and the torque remains <15% of the external force moment.

equator (increasing the filament's curvature) results in the coupling of its rotational and parallel motions.

It is also useful to describe this coupling of motions by inspecting the the mathematical structure of the fundamental solutions. Figure 5(c) shows variations of the off-diagonal component of periodic Green's function, $G_{\theta\phi}$ along the azimuthal direction at different distances from the equator. As can be seen, $G_{\theta\phi}$ is antisymmetric and increases in magnitude as we move towards the poles. Since $G_{\phi\theta}$ is an odd function with respect to ϕ, applying a uniform force in parallel ($\hat{\phi}$) direction of the filament in Eq. (1) produces a rotational flow around it; see full expressions in Appendix.

Figures 6(a), 6(b), and 6(c) show the variations of parallel drag of a filament with curvature κ to its parallel drag at the equator ($\xi_{\parallel}^{\kappa}/\xi_{\parallel}$) as a function of the filament's curvature, at different ratios of L/R and $\ell_0/R = 0.01$, 1, and 100. As shown earlier, when $\ell_0/R \ll 1$, the filament dynamics become independent of the membrane geometry, resulting in small (<10 %) increases in parallel drag with curvature, as shown in Fig. 6(a).

At $\ell_0/R = 100$, the parallel drag shows a significantly larger increase with the filament's curvature (up to 50 % increase), which can be explained as follows. The confinement flows are controlled by the membrane geometry, when $\ell_0/R \geqslant 1$. Larger curvatures represent larger displacements from the equator, corresponding to stronger flow confinements on the filament's side close to the poles, leading to larger drags. These flow confinement effects increase with increasing L/R, resulting

in larger positive deviations from the filament's drag on the equator. Nevertheless, these positive deviations remain of $O(1)$. This is consistent with our earlier observation that parallel motion is only weakly affected by the flow confinement effects. As shown in Fig. 2(c), the choice of $\ell_0/R = 1$ gives nearly the same results as $\ell_0/R = 100$, which shows the fluid flows are already dominated by membrane geometry in this limit.

Figures 6(d), 6(e), and 6(f) show the torque induced by the flow asymmetry vs the filament's curvature at $\ell_0/R = 0.01,\ 1$, and 100, respectively. The torque magnitudes, T, are nondimensionalized by their associated drag times membrane radius, $\xi_{\parallel}^{\kappa} UR$, which corresponds to the external torque on the system. In all cases, the torque monotonically increases with increasing curvature (κR) and L/R. This is to be expected, as the increase in both the filament's length and its curvature leads to stronger flow asymmetries.

V. CONCLUDING REMARKS

The transport and dynamic organization of biopolymers bound to the cell membrane occur in many cellular processes. Most studies on the hydrodynamics of inclusions in fluid interfaces have been on planar membranes and those studies that explore the effect of membrane geometry or curvature have not considered rodlike particles or filaments [33,35,37]. This work fills some of the gaps in the literature by computing the resistance or mobility of a single filament of constant curvature moving in a fluid spherical membrane, using a slender-body formulation. Our results show that the membrane spherical geometry influences the filament's dynamics in three distinct ways:

(1) As a consequence of the boundedness of spherical geometry, the momentum is transported from the interface to the 3D fluid domains over the length scale of the membrane's radius, when the radius is smaller than SD length. This behavior has also been discussed in Henle and Levine [36]. When the momentum transfer length is defined as the half of the harmonic average of SD length and membrane radius, $\ell^{\star} = (\ell_0^{-1} + R^{-1})^{-1}$, the computed parallel and rotational resistance values over a wide range of ℓ_0/R and L/R collapsed to the results of a planar membrane; see Figs. 2(a) to 2(f).

(2) We found that the combination of surface flow incompressibility and boundedness of spherical geometry gives rise to strong flow confinement effects [see Fig. 3(b)] that lead to large increases in the filament's perpendicular drag. These effects increase in magnitude with increasing L/R; see Figs. 2(g), 2(h), and 2(i). Related to this, we found that at $L/R > 1$, the resistance diverges with the inverse of gap size: $\xi_{\perp} \sim (\pi R/L - 1)^{-1}$; see Fig. 4(b). These effects cannot be mapped to planar membrane results by replacing ℓ_0 with $\ell^{\star}$.

(3) As a model for curvature sensors with a preferred curvature, such as BAR domains, we studied the case where the filament's curvature is constant along its length but larger than its minimum value $\kappa > R^{-1}$. We showed that this curvature mismatch generates asymmetric flows around the filament when it is translating along its axis [see Fig. 5(a)], resulting in a net torque on it. This coupling between the parallel and rotational motions of the filament is amplified by increasing the filament's curvature and length; see Figs. 6(d), 6(e), and 6(f).

A standard method for characterizing the rheology of the membrane and other fluid interfaces is to use their measured diffusion and the predicted values of mobility to extract the interface viscosity, η_m (or its linear viscoelastic response, if the generalized Stokes-Einstein relationship is used). When the particle is significantly smaller than SD length, the mobility (and diffusion) approaches Saffman's limit: $D = k_b T(1/4\pi\eta_m)[\ln(2\ell_0/a) - \gamma]$. Hence, large variations of particle or probe size and viscosity produce only weak variations in the diffusive motion. In the other limit of having a filament much larger than SD length moving in a planar membrane, the dynamics is dominated by the surrounding fluid and weakly dependent on membrane viscosity. This makes the rheological characterization of interfaces very challenging.

Using the filaments' motion on a spherical geometry may resolve some of these complications. As shown in Fig. 2(b), when the membrane radius is much smaller than SD length, $\ell_0/R \gg 1$, its dimensionless parallel drag $[\xi_{\parallel}/(4\pi\eta_{\mathrm{m}})]$ is independent of ℓ_0 and only a function of L/R. Note

that, as long as $\ell_0/R \gg 1$, the drag (including the rotational and perpendicular ones) is linearly dependent on η_m. This behavior is fundamentally different from the drag on planar membranes at $L/\ell_0 \gg 1$, which is weakly (logarithmic) dependent on η_m. Also, the dependency of $\xi_\parallel$ to L/R is significantly stronger than the logarithmic dependency of particles on planar membranes in the Saffman limit. Hence, varying the filament's length or the membrane radius is expected to provide larger changes in the diffusion (mobility) of the particles and more accurate measurements of η_m, compared to the experiments on planar membranes. Assuming membrane viscosity varies within the range $\eta_m \in [10^{-9},\ 10^{-6}]$ (Pa s m) [46], we have $\ell_0 \in [10^{-6},\ 10^{-3}]$ (m). Using vesicles or cells of a few microns in radius is likely to satisfy the condition of $\ell_0/R \gg 1$.

Surface incompressibility and the coupling of interfacial flows to the surrounding 3D fluid domains introduce several qualitative changes in HIs between the bound particles compared to particles in 3D fluids. These changes can result in novel emergent behaviors in the interface-bound suspensions [20,21,37]. Our work highlights one of these changes, namely the large difference between the mobility of filaments in the perpendicular and parallel directions when the filament's length is comparable to the membrane radius. Varying the ratio $\chi_\perp/\chi_\parallel$ is expected to lead to a qualitatively different organization of the filaments. Computational studies of suspensions of bound filaments are needed to explore some of these effects. The formulation and the results presented here form the basis for performing these simulations.

ACKNOWLEDGMENTS

We acknowledge support from the National Science Foundation under Grant No. 1944156.

APPENDIX: FULL EXPRESSIONS FOR THE GREEN'S FUNCTION IN SPHERICAL GEOMETRY

Here we outline the fundamental solutions to the system of Eqs. (2), in response to a point-force on the membrane at (θ_0, ϕ_0) on the sphere, where $\theta \in [0, \pi]$ is the polar angle and $\phi \in [0, 2\pi)$ is the azimuthal angle, defined in Fig. 1(a). The equations after including the externally applied point force are

$$\eta^\pm \nabla^2 \mathbf{u}^\pm - \nabla p^\pm = \mathbf{0}, \quad \nabla \cdot \mathbf{u}^\pm = 0, \tag{A1a}$$

$$\eta_m(\Delta_\gamma \mathbf{u}_m + K(\mathbf{x}_m)\mathbf{u}_m) - \nabla_\gamma p_m + \mathbf{T}|_{r=R} + \mathbf{f}^{\mathrm{ext}}\delta(\theta_0, \phi_0) = \mathbf{0}, \quad \nabla_\gamma \cdot \mathbf{u}_m = 0, \tag{A1b}$$

where $\delta(\theta_0, \phi_0)$ is a Dirac delta function. The analytical solutions to Eq. (A1) was provided by [35,36], which we reproduce here for completeness. The velocity field at an arbitrary point (θ, ϕ) is $\mathbf{u}(\theta, \phi) = \mathbf{G}(\theta, \phi, \theta_0, \phi_0) \cdot \mathbf{f}(\theta_0, \phi_0)$. Writing this expression in matrix form gives

$$\begin{bmatrix} u_\theta \\ u_\phi \end{bmatrix} = \frac{1}{4\pi\eta_m} \begin{bmatrix} G_{\theta\theta} & G_{\theta\phi} \\ G_{\phi\theta} & G_{\phi\phi} \end{bmatrix} \cdot \begin{bmatrix} f_\theta^{\mathrm{ext}}(\theta_0, \phi_0) \\ f_\phi^{\mathrm{ext}}(\theta_0, \phi_0) \end{bmatrix},$$

where

$$G_{\theta\theta} = \sum_{l=2}^{\infty} \frac{2l+1}{s_l l(l+1)} \Big[-P_l^2(\cos\psi) \sin^{-2}\psi \sin\theta \sin\theta_0 \sin^2(\phi - \phi_0) - P_l^1(\cos\psi) \sin^{-1}\psi \cos(\phi - \phi_0) \Big], \tag{A2a}$$

$$G_{\theta\phi} = \sum_{l=2}^{\infty} \frac{2l+1}{s_l l(l+1)} \Big\{ P_l^2(\cos\psi) \sin^{-2}\psi [-\cos\theta \sin\theta_0 + \sin\theta \cos\theta_0 \cos(\phi - \phi_0)] \times \sin\theta_0 \sin(\phi - \phi_0) - P_l^1(\cos\psi) \sin^{-1}\psi \cos\theta_0 \sin(\phi - \phi_0) \Big\}, \tag{A2b}$$

$$G_{\phi\theta} = \sum_{l=2}^{\infty} \frac{2l+1}{s_l l(l+1)} \Big\{ P_l^2(\cos\psi)\sin^{-2}\psi[\sin\theta\cos\theta_0 - \cos\theta\sin\theta_0\cos(\phi-\phi_0)] \times \sin\theta\sin(\phi-\phi_0) + P_l^1(\cos\psi)\sin^{-1}\psi\cos\theta\sin(\phi-\phi_0)\Big\}, \tag{A2c}$$

$$G_{\phi\phi} = \sum_{l=2}^{\infty} \frac{2l+1}{s_l l(l+1)} \Big\{ P_l^2(\cos\psi)\sin^{-2}\psi[-\cos\theta\sin\theta_0 + \sin\theta\cos\theta_0\cos(\phi-\phi_0)] \times [-\sin\theta\cos\theta_0 + \cos\theta\sin\theta_0\cos(\phi-\phi_0)] - P_l^1(\cos\psi)\sin^{-1}\psi[\sin\theta\sin\theta_0 + \cos\theta\cos\theta_0\cos(\phi-\phi_0)]\Big\}, \tag{A2d}$$

$$\cos\psi = \cos\theta\cos\theta_0 + \sin\theta\sin\theta_0\cos(\phi-\phi_0), \tag{A3}$$

and

$$s_l = l(l+1) - 2 + \frac{R}{\ell_-}(l-1) + \frac{R}{\ell_+}(l+2). \tag{A4}$$

Here $P_l^m(\cos\psi)$ is the associated Legendre polynomials with degree l and order m, $\ell_\pm = \eta_m/\eta^\pm$ and R is the radius of the sphere. Note that the summation of l in the Green's function starts from $l = 2$ where we exclude the rigid-body rotation term $l = 1$ because we consider only *relative* motion of filament with respect to the spherical membrane [36,37].

[1] F. Rizzelli, M. G. Malabarba, S. Sigismund, and M. Mapelli, The crosstalk between microtubules, actin and membranes shapes cell division, Open Biol. **10**, 190314 (2020).

[2] K. S. Cannon, B. L. Woods, J. M. Crutchley, and A. S. Gladfelter, An amphipathic helix enables septins to sense micrometer-scale membrane curvature, J. Cell Biol. **218**, 1128 (2019).

[3] M. Simunovic, A. Srivastava, and G. A. Voth, Linear aggregation of proteins on the membrane as a prelude to membrane remodeling, Proc. Natl. Acad. Sci. USA **110**, 20396 (2013).

[4] A. Kusumi, C. Nakada, K. Ritchie, K. Murase, K. Suzuki, H. Murakoshi, R. S. Kasai, J. Kondo, and T. Fujiwara, Paradigm shift of the plasma membrane concept from the two-dimensional continuum fluid to the partitioned fluid: High-speed single-molecule tracking of membrane molecules, Annu. Rev. Biophys. Biomol. Struct. **34**, 351 (2005).

[5] V. Prasad, S. A. Koehler, and E. R. Weeks, Two-Particle Microrheology of Quasi-2D Viscous Systems, Phys. Rev. Lett. **97**, 176001 (2006).

[6] T. Verwijlen, P. Moldenaers, H. A. Stone, and J. Vermant, Study of the flow field in the magnetic rod interfacial stress rheometer, Langmuir **27**, 9345 (2011).

[7] Z. A. Zell, A. Nowbahar, V. Mansard, L. G. Leal, S. S. Deshmukh, J. M. Mecca, C. J. Tucker, and T. M. Squires, Surface shear inviscidity of soluble surfactants, Proc. Natl. Acad. Sci. USA **111**, 3677 (2014).

[8] P. Saffman and M. Delbrück, Brownian motion in biological membranes, Proc. Natl. Acad. Sci. USA **72**, 3111 (1975).

[9] P. Saffman, Brownian motion in thin sheets of viscous fluid, J. Fluid Mech. **73**, 593 (1976).

[10] S. Ramadurai, A. Holt, V. Krasnikov, G. van den Bogaart, J. A. Killian, and B. Poolman, Lateral diffusion of membrane proteins, J. Am. Chem. Soc. **131**, 12650 (2009).

[11] T. T. Hormel, S. Q. Kurihara, M. K. Brennan, M. C. Wozniak, and R. Parthasarathy, Measuring Lipid Membrane Viscosity Using Rotational and Translational Probe Diffusion, Phys. Rev. Lett. **112**, 188101 (2014).

[12] Y. Gambin, R. Lopez-Esparza, M. Reffay, E. Sierecki, N. Gov, M. Genest, R. Hodges, and W. Urbach, Lateral mobility of proteins in liquid membranes revisited, Proc. Natl. Acad. Sci. USA **103**, 2098 (2006).

[13] A. Naji, A. J. Levine, and P. A. Pincus, Corrections to the Saffman-Delbrück mobility for membrane bound proteins, Biophys. J. **93**, L49 (2007).
[14] F. Quemeneur, J. K. Sigurdsson, M. Renner, P. J. Atzberger, P. Bassereau, and D. Lacoste, Shape matters in protein mobility within membranes, Proc. Natl. Acad. Sci. USA **111**, 5083 (2014).
[15] J. K. Sigurdsson, F. L. Brown, and P. J. Atzberger, Hybrid continuum-particle method for fluctuating lipid bilayer membranes with diffusing protein inclusions, J. Comput. Phys. **252**, 65 (2013).
[16] B. A. Camley and F. L. H. Brown, Contributions to membrane-embedded-protein diffusion beyond hydrodynamic theories, Phys. Rev. E **85**, 061921 (2012).
[17] E. Evans and E. Sackmann, Translational and rotational drag coefficients for a disk moving in a liquid membrane associated with a rigid substrate, J. Fluid Mech. **194**, 553 (1988).
[18] H. A. Stone and A. Ajdari, Hydrodynamics of particles embedded in a flat surfactant layer overlying a subphase of finite depth, J. Fluid Mech. **369**, 151 (1998).
[19] N. Oppenheimer and H. Diamant, Correlated diffusion of membrane proteins and their effect on membrane viscosity, Biophys. J. **96**, 3041 (2009).
[20] N. Oppenheimer, D. B. Stein, and M. J. Shelley, Rotating Membrane Inclusions Crystallize Through Hydrodynamic and Steric Interactions, Phys. Rev. Lett. **123**, 148101 (2019).
[21] H. Manikantan, Tunable Collective Dynamics of Active Inclusions in Viscous Membranes, Phys. Rev. Lett. **125**, 268101 (2020).
[22] A. J. Levine, T. B. Liverpool, and F. C. MacKintosh, Dynamics of Rigid and Flexible Extended Bodies in Viscous Films and Membranes, Phys. Rev. Lett. **93**, 038102 (2004).
[23] C. Klopp, R. Stannarius, and A. Eremin, Brownian dynamics of elongated particles in a quasi-two-dimensional isotropic liquid, Phys. Rev. Fluids **2**, 124202 (2017).
[24] H. Manikantan and T. M. Squires, Surfactant dynamics: Hidden variables controlling fluid flows, J. Fluid Mech. **892**, P1 (2020).
[25] T. M. Fischer, The drag on needles moving in a Langmuir monolayer, J. Fluid Mech. **498**, 123 (2004).
[26] L. Scriven, Dynamics of a fluid interface equation of motion for Newtonian surface fluids, Chem. Eng. Sci. **12**, 98 (1960).
[27] T. W. Secomb and R. Skalak, Surface flow of viscoelastic membranes in viscous fluids, Q. J. Mech. Appl. Math. **35**, 233 (1982).
[28] G. M. Mavrovouniotis and H. Brenner, A micromechanical investigation of interfacial transport processes. I. Interfacial conservation equations, Philos. Trans. R. Soc London A **345**, 165 (1993).
[29] G. M. Mavrovouniotis, H. Brenner, D. A. Edwards, and L. Ting, A micromechanical investigation of interfacial transport processes. II. Interfacial constitutive equations, Philos. Trans. R. Soc. London A **345**, 209 (1993).
[30] F. G. Woodhouse and R. E. Goldstein, Shear-driven circulation patterns in lipid membrane vesicles, J. Fluid Mech. **705**, 165 (2012).
[31] A. R. Honerkamp-Smith, F. G. Woodhouse, V. Kantsler, and R. E. Goldstein, Membrane Viscosity Determined from Shear-Driven Flow in Giant Vesicles, Phys. Rev. Lett. **111**, 038103 (2013).
[32] D. Nelson, T. Piran, and S. Weinberg, *Statistical Mechanics of Membranes and Surfaces* (World Scientific, Toh Tuck Link, Singapore, 2004).
[33] J. K. Sigurdsson and P. J. Atzberger, Hydrodynamic coupling of particle inclusions embedded in curved lipid bilayer membranes, Soft Matter **12**, 6685 (2016).
[34] D. A. Rower, M. Padidar, and P. J. Atzberger, Surface fluctuating hydrodynamics methods for the drift-diffusion dynamics of particles and microstructures within curved fluid interfaces, J. Comput. Phys. **455**, 110994 (2022).
[35] M. L. Henle, R. McGorty, A. Schofield, A. Dinsmore, and A. Levine, The effect of curvature and topology on membrane hydrodynamics, EPL (Europhys. Lett.) **84**, 48001 (2008).
[36] M. L. Henle and A. J. Levine, Hydrodynamics in curved membranes: The effect of geometry on particulate mobility, Phys. Rev. E **81**, 011905 (2010).
[37] R. Samanta and N. Oppenheimer, Vortex flows and streamline topology in curved biological membranes, Phys. Fluids **33**, 051906 (2021).

[38] J. Happel and H. Brenner, *Low Reynolds Number Hydrodynamics: With Special Applications to Particulate Media*, vol. 1 (Springer Science & Business Media, Hingham, MA, 2012).

[39] S. Kim and S. J. Karrila, *Microhydrodynamics: Principles and Selected Applications* (Courier Corporation, Stoneham, MA, 2013).

[40] S. Bagaria and R. Samanta, Dynamics of force dipoles in curved biological membranes, arXiv:2110.05460 (2021).

[41] See Supplemental Material at http://link.aps.org/supplemental/10.1103/PhysRevFluids.7.084004 for detailed methods and extra data. In Sec. I we readdress the formulation we use to compute the resistances. In Sec. II we compare the difference between two numerical methods. In Sec. III we analyze the errors resulting from numerical implementation. In Sec. IV we evaluate the errors due to the finite thickness of the filament. In Sec. V we quantify the positive deviations of parallel resistance from planar membrane values.

[42] A.-K. Tornberg and M. J. Shelley, Simulating the dynamics and interactions of flexible fibers in Stokes flows, J. Comput. Phys. **196**, 8 (2004).

[43] E. Nazockdast, A. Rahimian, D. Zorin, and M. Shelley, A fast platform for simulating semi-flexible fiber suspensions applied to cell mechanics, J. Comput. Phys. **329**, 173 (2017).

[44] J. Lighthill, Flagellar hydrodynamics, SIAM Rev. **18**, 161 (1976).

[45] R. E. Johnson, An improved slender-body theory for Stokes flow, J. Fluid Mech. **99**, 411 (1980).

[46] Y. Sakuma, T. Kawakatsu, T. Taniguchi, and M. Imai, Viscosity landscape of phase-separated lipid membrane estimated from fluid velocity field, Biophys. J. **118**, 1576 (2020).